Article

One-Dimensional Copper-Doped Rb$_2$AgI$_3$ with Efficient Sky-Blue Emission as a High-Performance X-ray Scintillator

Jiali Yao, Dan Huang, Xudong Hu, Haiming Cheng, Dayang Wang, Xiaoming Li,* Wensheng Yang,* and Renguo Xie*
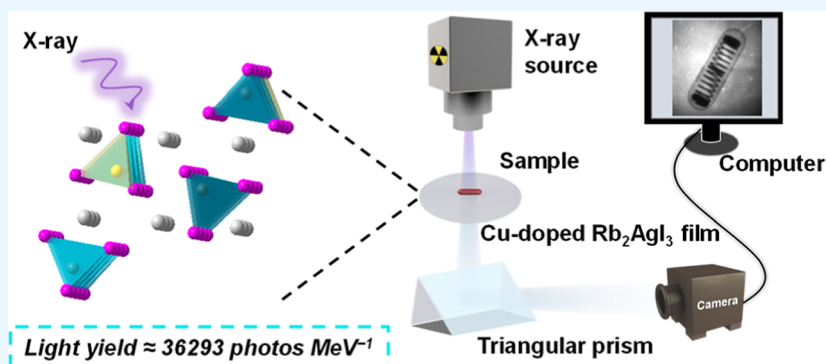
Cite This: ACS Omega 2024, 9, 28969−28977

Read Online

ACCESS | Metrics & More | Article Recommendations | Supporting Information

Light yield ≈ 36293 photos MeV^{-1}

ABSTRACT: Scintillators have garnered heightened attention for their diverse applications in medical imaging and security inspection. Nonetheless, commercial scintillators encounter challenges with costly rare-earth metals and toxic elements like thallium (Tl), driving the need for sustainable, cost-effective, and eco-friendly alternatives to meet contemporary X-ray detection demands. This study focuses on exploring the potential of Cu$^+$-doped Rb$_2$AgI$_3$ as an effective metal halide (MH) scintillator. One-dimensional (1D) Rb$_2$AgI$_3$ and Cu$^+$-doped Rb$_2$AgI$_3$ single crystals (SCs) were synthesized by using the conventional temperature-lowering crystallization method. When excited by UV light, Cu$^+$-doped SCs emitted a broad sky-blue light at 490 nm with a high photoluminescence (PL) quantum yield (PLQY) of 76.48%. Remarkably, under X-ray excitation, these Cu$^+$-doped SCs demonstrated an outstanding light yield of 36,293 photons MeV^{-1}, a relatively low detection threshold of 1.022 μGy$_{air}$ s^{-1}, and a rapid scintillation decay time of 465 ns. The prepared translucent scintillation film has good uniformity and flexibility, with a high spatial resolution of 10.2 lp mm^{-1}. These results position Cu$^+$-doped Rb$_2$AgI$_3$ as a leading candidate among promising X-ray scintillators, offering superior scintillation light yield, excellent stability, and nontoxicity.

1. INTRODUCTION

Scintillators are indispensable for converting high-energy photons, including X-rays, into luminescence, playing a crucial role across diverse applications such as medical diagnosis, security inspection, and electronic industries.[1−3] Commercial radiation detectors extensively rely on traditional scintillator materials, including NaI: Tl, CsI: Tl, Lu$_3$Al$_5$O$_{12}$: Ce, and Bi$_4$Ge$_3$O$_{12}$.[4−7] However, these materials present substantial challenges. Primarily, they often require the introduction of either toxic thallium (Tl) or expensive rare-earth ions as activators incorporated into the forbidden gap of the host to achieve the conversion of X-rays to visible light. Simultaneously, certain commercial scintillators that possess luminescent host lattices exhibit characteristics of self-activated emission. For instance, Bi$_4$Ge$_3$O$_{12}$, serving as a radiation-resistant scintillator, exhibits self-quenching in light output when exposed to X-ray doses exceeding 10^6 to 10^7 rad.[8] This intrinsic limitation significantly constrains their practical application in environments characterized by high-dose radiation. Furthermore, the synthesis of typical commercial scintillator materials often requires high temperatures within a vacuum environment, presenting obstacles to cost-effective and environmentally friendly synthesis.[9] In essence, the essential attributes of an ideal scintillator include high-light yields, fast response time, low cost, and simple fabrication.

Recently, metal halides (MHs) have emerged as a promising class of optoelectronic materials, demonstrating successful applications in various devices, including light-emitting diodes, lasers, solar cells, and X-ray scintillators.[10−15] The use of MHs

as scintillator materials was first reported in the 1990s,[16,17] and this interest has been renewed in recent years due to the remarkable success of MHs as high-light yield, good spectral stability, and low-cost scintillators. Liu and co-workers developed a flexible prototype device for multicolor X-ray scintillation from three types of perovskite nanocrystal scintillators, CsPbBr$_2$I, CsPbBr$_3$, and CsPbClBr$_2$,[18] showing strong X-ray absorption and intense radioluminescence (RL) in visible wavelengths. Despite the advantages of lower toxicity and low-temperature synthesis in CsPbX$_3$ (X = Cl, Br, and I) nanocrystals over traditional CsI: Tl scintillators, concerns about Pb toxicity persist due to the ionic nature and high solubility of lead-based halide perovskites in water.[19] Exploring alternatives, including lead-free perovskites and other halide scintillators, is essential to address these concerns.

To address these challenges, researchers have successfully developed environmentally friendly, lead-free MH, including Cu(I), Sn(II), Mn(II), In(III), Bi(III), Sb(III), and Hf(IV)-based MHs.[13,20−27] Among them, Cu-based MH scintillators emerge as the most researched and superior performers in terms of scintillation properties. Tang and co-workers reported a series of scintillation properties of CsCu$_2$I$_3$, Cs$_3$Cu$_2$I$_5$, and A$_2$CuX$_3$ (A = Rb and K; X = Cl and Br) with a comparable light yield of 21,580−79,279 photons MeV^{-1}, demonstrating that Cu-based MHs might be potential scintillators for low cost, large area, and flexible X-ray imaging.[28−32] The extended carrier decay time observed in Cu-based MH scintillators, typically in the order of microseconds, limits their real-time detection capabilities.[28] Given that the material's effectiveness in X-ray absorption and detection sensitivity is primarily determined by its effective atomic number, addressing this challenge becomes crucial.[33] Ag-based MHs, with a higher atomic number and shorter decay time compared to Cu-based MHs, make them potential candidates for enhanced performance in X-ray detection. Our previous work reported a light yield of ∼27,000 photons MeV^{-1} and a fast scintillation decay time of 288 ns in Cu$^+$-doped Cs$_2$AgI$_3$ for the first time.[34] Subsequently, Mohammed and co-workers adopted this material to fabricate flexible, large-area scintillation screens with a resolution of 16.2 lp/mm, exhibiting excellent X-ray scintillation performance.[35]

In this article, the 1D Rb$_2$AgI$_3$ and Cu$^+$-doped Rb$_2$AgI$_3$ SCs have been synthesized through the typical temperature-lowering crystallization method. The introduction of Cu$^+$ renders the Rb$_2$AgI$_3$ SCs an intense sky-blue emission that peaked at ∼490 nm with a high PLQY of 76.48%, a characteristic that is absent in the undoped material at ambient temperature. Both experimental and theoretical investigations suggest that the origin of the sky-blue emission may be attributed to self-trapped excitons (STEs). Consequently, Cu$^+$-doped Rb$_2$AgI$_3$ SCs were explored as a new generation of MH scintillator materials,[13,22] with a rapid scintillation decay time of 465 ns, a relatively low detection limit of 1.022 μGy_{air} s^{-1}, and a high-light yield of 36,293 photons MeV^{-1} under X-ray irradiation. The light yield of scintillators emerges as a crucial determinant influencing the X-ray conversion efficiency and detection contrast. Our findings indicate that the light yield of Cu$^+$-doped Rb$_2$AgI$_3$ SCs surpasses that of Cu$^+$-doped Cs$_2$AgI$_3$ SCs. In addition, Cu$^+$-doped Rb$_2$AgI$_3$ SCs also exhibited outstanding stability in ambient air and excellent radiative stability at a high X-ray dose rate. The Cu$^+$-doped Rb$_2$AgI$_3$ film exhibits excellent flexibility and high-performance X-ray imaging with a high spatial

resolution of 10.2 lp mm^{-1}. These results indicate that Cu$^+$-doped Rb$_2$AgI$_3$ SCs exhibit stability, environmental friendliness, rapid decay time, high-light yield, and high PLQY. These properties have potential implications for advancements in emitting optoelectronic fields and X-ray imaging applications.

2. EXPERIMENTAL SECTION

2.1. Materials. Rubidium iodide (RbI, 99.8%), silver iodide (AgI, 99.999%), cuprous iodide (CuI, 98%), and hypophosphorous acid (AR, 50 wt % in H$_2$O) were purchased from Aladdin Industrial Corporation. Polydimethylsiloxane (PDMS) and platinum divinyltetramethyldisiloxane solutions were purchased from Dow Corning. Hydroiodic acid (HI, 38 wt %/wt aq sol.) was purchased from Sinopharm Chemical Reagent Co., Ltd. Toluene was purchased from Thermo Fisher Scientific. All chemical agents were used without further purification.

2.2. Synthesis of Rb$_2$AgI$_3$ and Cu$^+$-Doped Rb$_2$AgI$_3$ SCs. The single crystals (SCs) of Rb$_2$AgI$_3$ and Cu$^+$-doped Rb$_2$AgI$_3$ SCs were synthesized by using a solution cooling method. To prepare Rb$_2$AgI$_3$ SCs, RbI (0.6856 g, 2 mmol) and AgI (0.099 g, 1 mmol) were dissolved in a mixed solution of 2 mL of HI acid in a 20 mL glass bottle. The precursor was dissolved completely at 70 °C and cooled to room temperature on a heat plate. The resulting crystals were then washed with isopropanol to remove any residual HI and unreacted precursors, followed by drying under vacuum.

For Cu$^+$-doped Rb$_2$AgI$_3$ SCs, AgI was replaced with CuI according to the specified percentage ratio for the replacement. The feed molar ratios of Cu/(Cu + Ag) were set at 0.05, 0.1, 0.15, and 0.2. In addition, 0.5 mL of hypophosphorus acid was added to prevent Cu$^+$ oxidation. All other conditions remained the same.

2.3. Synthesis of Cu$^+$-Doped Rb$_2$AgI$_3$@PDMS Flexible Thin Films. For evaluating the RL performance, we fabricated Cu$^+$-doped Rb$_2$AgI$_3$@PDMS scintillator films. First, the Rb$_2$AgI$_3$ SCs were ground into a fine powder using a mortar and pestle. Subsequently, mixing PDMS, curing agent (platinum divinyltetramethyldisiloxane solution), and 1.72% Cu$^+$:Rb$_2$AgI$_3$ powder in a glass bottle at a ratio of 3 g:0.3 g:1 g followed by continuous stirring for 10 h at room temperature, resulted in a homogeneous mixture. Finally, this mixture was introduced into a quartz container and left to naturally form a film.

2.4. Measurement and Characterization. Powder X-ray diffraction (XRD) pattens for all samples were collected with a Philips PW1830 X-ray diffractometer with Cu K$_\alpha$ radiation (λ = 0.154056 nm). ICP analysis was conducted on an ICP-OES (Optima 3300DV). A scanning electron microscope (SEM) (SU8020, Hitachi) equipped with an energy dispersive spectrometer (EDS) was adopted to collect composition and the elemental mappings. The UV−vis absorption spectra were measured by Shimadzu UV-2600, where the crystal was ground as powder for testing in the range from 220 to 800 nm. The PL, PLE, time-resolved PL, and temperature-dependent PL spectra of all samples were measured by a steady-state fluorescence spectrometer (Edinburgh FLS920). The PLQY measurements were performed in the FLS920 fluorescence spectrometers with a xenon lamp and a Quanta-φ integrating sphere.

2.5. DFT Methods. All density functional theory (DFT) calculations were performed utilizing the Vienna Ab initio
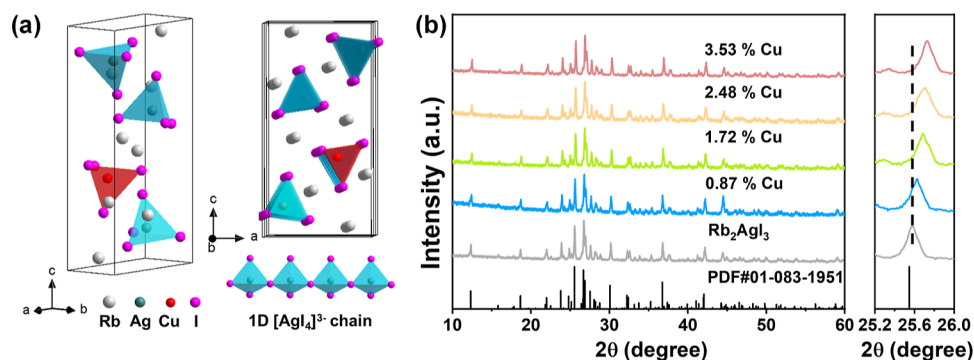
Figure 1. (a) Diagram of the crystal structure of Cu^+-doped Rb_2AgI_3. (b) XRD patterns of xCu^+: Rb_2AgI_3 (x = 0.87, 1.72, 2.48, and 3.52%) and the zoomed-in XRD patterns of the (121) diffraction peaks.
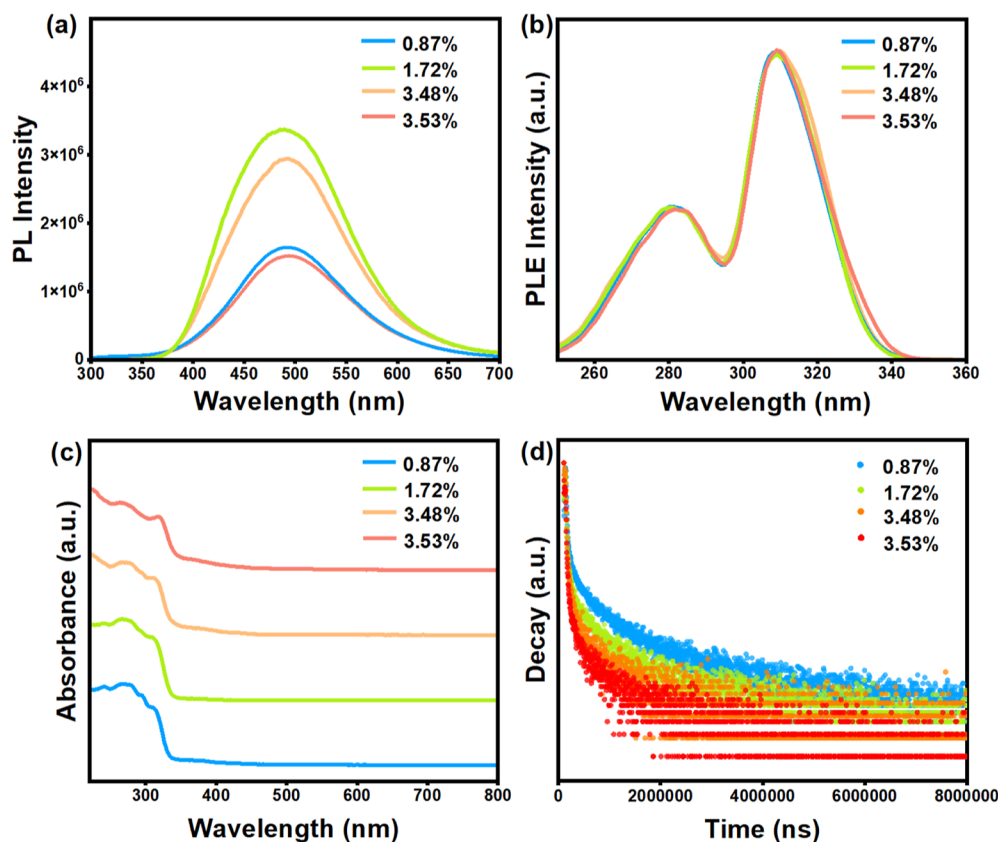
**Figure 2.** (a) PL spectra of xCu^+: Rb_2AgI_3 samples (λ_{ex} = 310 nm). (b) PLE spectra of xCu^+: Rb_2AgI_3 samples (λ_{em} = 490 nm). (c) Absorption spectra of xCu^+: Rb_2AgI_3 samples. (d) Time-resolved PL spectra at an emission wavelength of 490 nm of the xCu^+: Rb_2AgI_3 samples excited under 310 nm (x = 0.87, 1.72, 2.48, and 3.52%).

Simulation Package (VASP).[36,37] The exchange−correlation effects were described using the generalized gradient approximation (GGA) with the Perdew−Burke−Ernzerhof (PBE) functional.[38,39] The core−valence interactions were calculated within the projected augmented wave (PAW) method.[40] The PAW was set with a plane wave cutoff of 450 eV. Structural optimization was carried out, ensuring energy convergence below 1.0×10^{-6} eV and force convergence below 0.02 eV $Å^{-1}$. The bulk of Rb_2AgI_3 was constructed with lattice parameters of a = 10.204 Å, b = 4.859 Å, c = 19.892 Å, and $\alpha = \beta = \gamma = 90°$. The bulk of $Rb_2Cu_{0.25}Ag_{0.75}I_3$ was constructed with lattice parameters of a = 10.198 Å, b = 4.818 Å, c = 19.786 Å, and $\alpha = \beta = \gamma = 90°$. Electronic structure calculations for Rb_2AgI_3 and $Rb_2Cu_{0.25}Ag_{0.75}I_3$ utilized Brillouin

zone sampling with a 5 × 10 × 3 grid centered at the gamma (Γ) point. A Hubbard-type U parameter $(GGA + U)^{[41]}$ was added to correct the on-site Coulomb interactions, with $U[Cu]$ = 5.0 eV.[29]

2.6. Light Yield Measurement. CsI: Tl was used as a reference with a light yield of 54,000 photons MeV^{-1} under 50 keV X-ray. The scintillator adhered to the circular window of the integrating sphere at a consistent distance from the X-ray source. The corresponding RL spectra were recorded by a QE Pro fiber coupled fluorescence spectrometer. All characterizations were conducted under the condition of grinding the crystals into a fine powder. The light yield of the Cu^+-doped Rb_2AgI_3 scintillator was determined to be 36,293 photons MeV^{-1} by comparing the integral intensity of the two spectra.
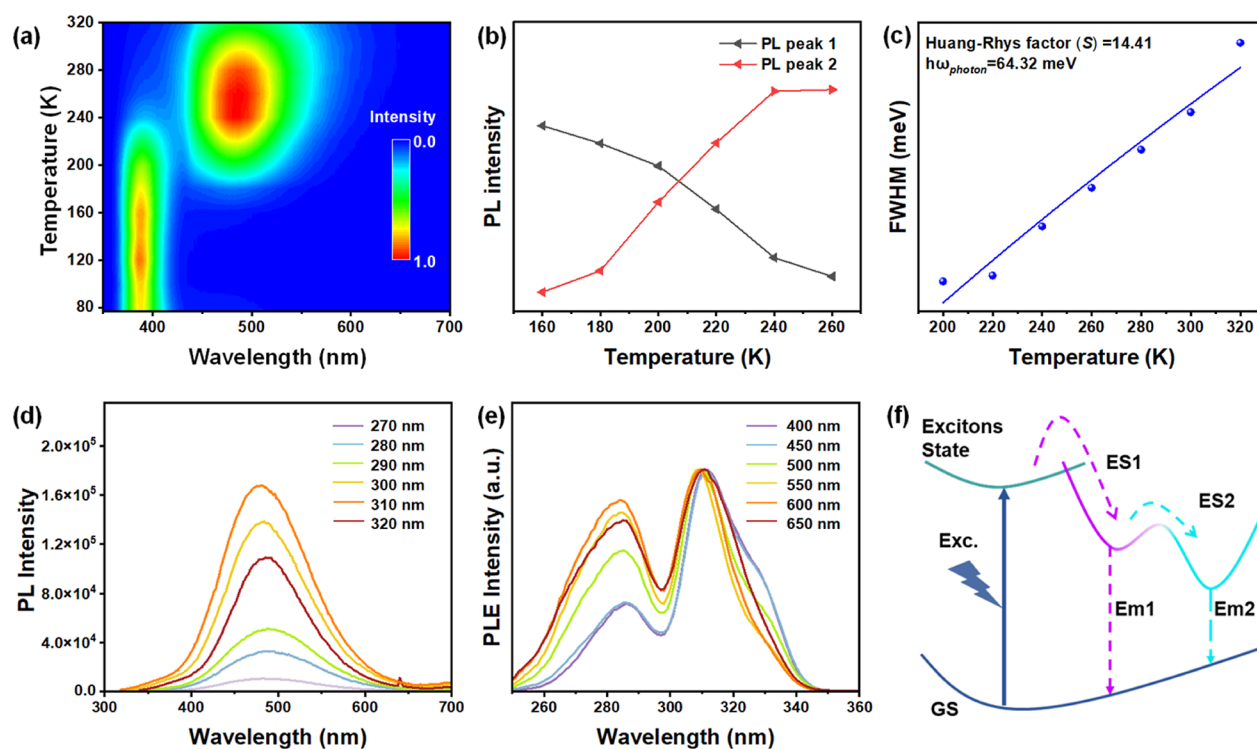
Figure 3. (a) Temperature-dependent PL spectra of 1.72% Cu⁺: Rb₂AgI₃ from 77 to 320 K (λ_{ex} = 310 nm). (b) Emission peak intensities of PL peak 1 and PL peak 2 within the temperature range of 160−260 K. (c) Fitting results of the fwhm as a function of temperature. PL spectra (d) and PLE spectra (e) of 1.72% Cu⁺: Rb₂AgI₃ measured various excitations and emissions, respectively. (f) Schematic diagram of possible luminescence mechanisms.

The detection limit was confirmed using indirect imaging techniques by a CMOS camera (FL-20BW, Tucsen Photonics Co., Ltd.) with 3 times the signal-to-noise ratio (SNR).

3. RESULTS AND DISCUSSION

The synthesis of Rb₂AgI₃ and Cu⁺-doped Rb₂AgI₃ SCs was carried out using temperature-lowering crystallization. Briefly, stoichiometric amounts of RbI, AgI, and CuI were dissolved in HI aqueous solution by heating at 70 °C on a hot plate. When the solution became transparent, it was slowly cooled down to room temperature. Nonluminescent Rb₂AgI₃ and bright sky-blue emissive Cu⁺-doped SCs were generated during the cooling process. As shown in Figure S1, 1D rod-like Cu⁺-doped Rb₂AgI₃ SCs were obtained with an average size of 1−2 cm in length and 200−300 μm in diameter, and the crystals emitted bright sky-blue light under 302 nm ultraviolet light irradiation. The crystal yield is about 47 ± 5%. Full details of the synthesis procedure are provided in the Experimental Section. According to the previous report,[42] pristine Rb₂AgI₃ possesses a 1D ribbon-like crystal structure, where the Ag atom is coordinated by four I atoms to form the [AgI₄]³⁻ units, and the Ag−I tetrahedron is connected through a shared corner. The 1D Ag−I chain is then separated from other chains by a Rb atoms. According to the structure refinement result, when doped Cu⁺, [AgI₄]³⁻ units were replaced by [CuI₄]³⁻ units, but the structure remained unchanged (Figure 1a). The structure and crystallinity of the as-synthesized crystals were confirmed from their powder XRD patterns. As shown in Figure 1b, the diffraction peaks are in accordance well with the standard orthorhombic Rb₂AgI₃ (PDF# 01-083-1951), and no impurity phases were detected, which indicates that the as-prepared sample is phase pure and has the orthorhombic space group

$Pnma$ (a = 10.2376 Å, b = 4.89791 Å, c = 19.9838 Å, and $\alpha = \beta = \gamma$ = 90°).[43] As the amount of Cu⁺ doping increases, the XRD peak gradually moves to a higher angle, proving that Cu⁺ substitutes for Ag⁺ with a smaller ionic radius (Cu⁺, r = 0.77 Å; Ag⁺, r = 1.26 Å). The chemical composition of the products was determined by inductively coupled plasma optical emission spectrometry (ICP-OES). The ICP-OES-determined Cu/(Cu + Ag) concentrations are 0.87, 1.72, 2.48, and 3.53%, while the feeding concentrations are 5, 10, 15, and 20%, respectively (Table S1). In addition, the chemical compositions (Rb, Ag, Cu, and I) of 1.72% Cu⁺: Rb₂AgI₃ were further identified from the energy dispersive X-ray spectroscopy (EDS) (Figure S2). The atomic percentages of elements are 33.12% for Rb, 15.54% for Ag, 0.18% for Cu, and 51.16% for I, respectively. The discrepancy between the actual doping ratio of Cu⁺ and the feeding ratio was because of the impurity ion lattice solubility and reaction conditions.[44] However, the fluorescence performance of the Cu⁺-doped samples remained unaffected. From the XRD and ICP-OES results, we speculate that Cu⁺ was incorporated in the Rb₂AgI₃ SCs successfully.

We then investigated the optical properties of undoped and Cu⁺-doped Rb₂AgI₃ SCs. As shown in Figure 2a, the optical properties of Cu⁺-doped Rb₂AgI₃ SCs have been systematically characterized. Upon irradiation at 310 nm, Cu⁺-doped Rb₂AgI₃ SCs display a broad sky-blue emission band at 490 nm with a fwhm of 140 nm. All emission shapes remain consistent at different doping amounts, and the emission light intensity first increased with the growth of Cu⁺ contents and then declined after reaching the maximum at 1.72% Cu⁺ with a high PLQY of approximately 76.48% (Figure S3). Figure S4 illustrates the evolution of the PLQY for xCu⁺: Rb₂AgI₃ (x = 0.87, 1.72, 2.48, and 3.52%) samples under an excitation wavelength of 310 nm.
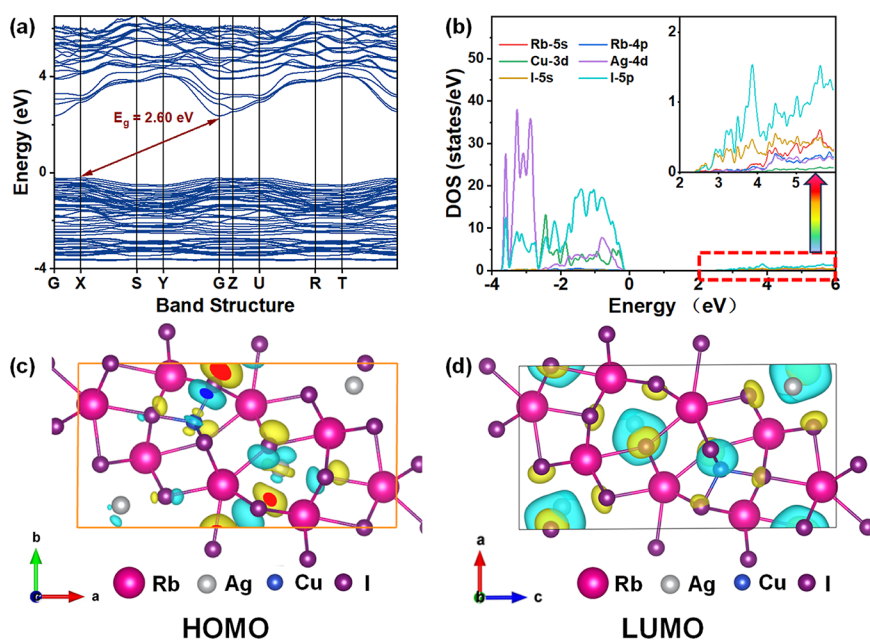
Figure 4. Band structures of Cu$^+$-doped Rb$_2$AgI$_3$ (a) and the corresponding density of states (DOS) (b) of Cu$^+$-doped Rb$_2$AgI$_3$. Charge density maps of VBM (c) and CBM (d) of Cu$^+$-doped Rb$_2$AgI$_3$.

The normalized PL excitation (PLE) spectra exhibit two distinct excitation peaks at 280 and 310 nm, and the shape of the excitation peaks remains relatively consistent across various doping concentrations (Figure 2b). This observation suggests that the PL emission in Cu$^+$-doped Rb$_2$AgI$_3$ may originate from the same state of relaxation. Absorption spectra of Cu$^+$-doped Rb$_2$AgI$_3$ SCs show that the absorption edge of pristine Rb$_2$AgI$_3$ is about 310 nm (Figure S5). For Cu$^+$-doped Rb$_2$AgI$_3$ SCs, the absorption edge exhibits a red-shift to 335 nm (Figure 2c), and the absorption band edge further red-shifts with the increasing doping concentration of copper. This observation is consistent with our doping concentration results obtained from ICP-OES and XRD analyses conducted previously. The PL decay curves of Cu$^+$-doped Rb$_2$AgI$_3$ SCs, fitted by the binary exponential equation in Figure 2d, revealed a gradual increase in decay time with an increasing doping level. Specifically, the decay times were 394 ns for the sample of 0.87%, 465 ns for the sample of 1.72%, 591 ns for the sample of 2.48%, and 792 ns for the sample of 3.52%. These results indicate that the introduction of Cu$^+$ ions significantly promotes the radiative recombination of STEs in Cu$^+$-doped Rb$_2$AgI$_3$ SCs.[35] All Cu$^+$-doped Rb$_2$AgI$_3$ SCs exhibit a relatively short lifetime in the nanosecond range, significantly shorter than the lifetimes of Cu-based MHs, which typically fall within the microsecond range002E

To further investigate the intrinsic emission mechanism, temperature-dependent PL spectra were recorded for 1.72% Cu$^+$: Rb$_2$AgI$_3$ SCs in the range of 77–320 K (Figure 3a). Surprisingly, it observed two emission peaks as the temperature decreased, and this emission character is a strong indicator of ion luminescence. With increasing temperature, both PL peaks red shift slightly, and the emission energy decreases, which may be due to the thermal expansion and electron–phonon interaction. As the temperature decreased, the emission peak intensity at ∼380 nm (peak 1) gradually rose, the emission peak intensity at ∼490 nm (peak 2) gradually decreased (Figures 3b and S6), and the fwhm decreased gradually, indicating that more photons are coupled with excitons, thus

activating the nonradiative recombination process at higher temperatures. The temperature-dependent PL decay curve of 1.72% Cu$^+$: Rb$_2$AgI$_3$ SCs was measured at 77 K, and the lifetime increased to 3.33 μs compared to that at 298 K (Figure S7). At cryogenic temperatures, the reduction in thermally activated quenching by trap (surface) states associated with short PL decay leads to a relative increase in the radiative transition probability. Conversely, at higher temperatures, the transition and recombination processes of photogenerated electrons are accelerated due to phonon assistance, resulting in shorter PL decay.[45] The Huang–Rhys factor (S) and the phonon frequency ($\hbar\omega_{\text{photon}}$) can be derived by the following equation[46]

$$\text{fwhm} = 2.36\sqrt{S}\,\hbar\omega_{\text{photon}}\sqrt{\coth\frac{\hbar\omega_{\text{photon}}}{2k_{\text{B}}T}}$$

By fitting the temperature-dependent fwhm curve, the S factor is derived as 14.41, and the $\hbar\omega_{\text{photon}}$ is 64.32 meV (Figure 3c). The Huang–Rhys factor is much larger than the traditional materials, such as CdSe and CdTe.[47,48] In addition, the resulting $\hbar\omega_{\text{photon}}$ agrees well with the displacement of an eigenvector, which originates from the Jahn–Teller distortion of the lattice. For the representative 1.72% Cu$^+$: Rb$_2$AgI$_3$ sample, the PL spectra at different exicitation wavelengths from 270–320 nm (Figure 3d) and the excitation-independent PL (PLE) spectra at different PL wavelengths from 400–650 nm (Figure 3e) show negligible peak shift or shape change, indicating that the broad emission originates from the same characteristics of ion luminescence and not from defect recombination centers. Combined with the large Stokes shift, large Huang–Rhys factor, and phonon frequency, the emission mechanism of Cu$^+$-doped Rb$_2$AgI$_3$ may be due to the formation of the STEs again.[49]

Two emission peaks can be detected at low temperatures ranging from 77 to 280 K, with a weak peak at 490 nm and another at 380 nm. The temperature-dependent dual emissions indicate that the emissions may not originate from the single
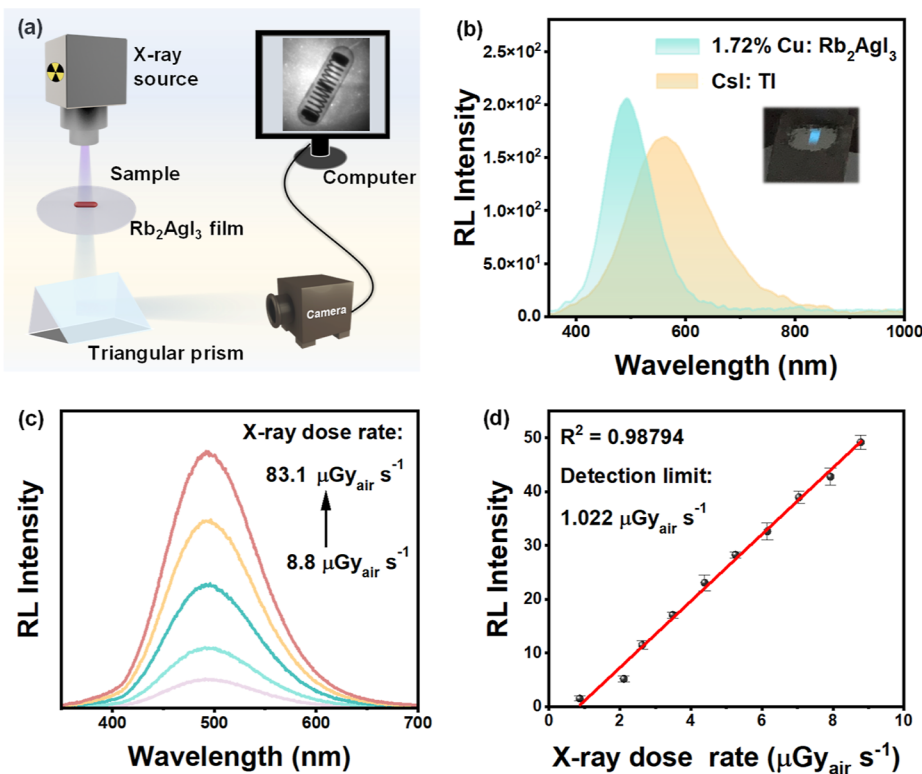
Figure 5. (a) Schematic diagram of our self-built X-ray imaging system. (b) RL spectrum of 1.72% Cu$^+$: Rb$_2$AgI$_3$ under 50 keV X-ray excitation. Inset shows the photograph of the 1.72% Cu$^+$: Rb$_2$AgI$_3^+$ powder under X-ray. (c) RL emission spectra recorded at different dose rates in the range of 8.8–83.1 μGy$_{air}$ s^{-1}. (d) Linear response curve toward X-rays.

excited state but from multiple radiative mechanisms, indicating the presence of two distinct excitonic states. To confirm the origin of the 380 nm emission, PL and PLE characterizations were performed on pristine Rb$_2$AgI$_3$ at 77 K. The pristine Rb$_2$AgI$_3$ SCs exhibit emission centered at 380 nm (Figure S8), which is consistent with the emission peak1. In fact, there have been few reports on the luminescence properties of pristine Rb$_2$AgI$_3$, with one study reporting its blue-green emission under UV excitation.[50] However, the Rb$_2$AgI$_3$ crystals we prepared did not show emission in visible light. Interestingly, we found that when crystals were ground with HI, blue-green emission was indeed obtained, possibly indicating a correlation with defects within the crystals. Therefore, we believe that the violet emission at 380 nm is from Rb$_2$AgI$_3$ intrinsic emission and the emission at 490 nm resulted from a Cu$^+$-related exciton state due to the successful replacement of Ag by Cu. This suggests the presence of two energy states with slight differences on the excited-state potential energy surface. At low temperatures, low thermal energy and soft lattice distortion make the excitons localized in the STEs state 1 (ES1), and it is hard to overcome the energy barrier to reach the STEs state 2 (ES2), resulting in the emission of 380 nm. With the increasing temperature (from 140 to 300 K), large lattice distortion and enough thermal energy make it easy for excitons to overcome the energy barrier to reach the ES2, resulting in the blue emission. Based on the discussion above, the schematic diagram of the Cu$^+$-doped Rb$_2$AgI$_3$ crystal is shown in Figure 3f.

In order to understand the electronic structure and luminescence mechanism of Rb$_2$AgI$_3$ and Cu$^+$-doped Rb$_2$AgI$_3$, DFT first-principles calculations were performed. Pristine Rb$_2$AgI$_3$ shows a distinct indirect band gap property

with a theoretical band gap value is about 2.6528 eV with the valence band maximum (VBM) at the X point and the conduction band minimum (CBM) at the G point in the first Brillouin zone (Figure S9a), which is consistent with the previous report.[50] The VBM and the CBM of pristine Rb$_2$AgI$_3$ are mainly composed of I-p, Ag-d orbitals and Ag-d, I-p orbitals, respectively (Figure S9b). Cu$^+$-doped Rb$_2$AgI$_3$ also shows a distinct indirect band gap characteristic with a value of 2.5962 eV, with VBM at the X point and CBM at the G point in the first Brillouin zone (Figure 4a). The smaller calculated band gap than the experimental value obtained from UV−vis absorption is a normal phenomenon because standard DFT calculations usually underestimate the band gap of the material.[51,52] The calculated density of states (DOS) of Cu$^+$-doped Rb$_2$AgI$_3$ is given in Figure 4b. From the total and projected DOS, the VB is contributed by the Ag-4d, Cu-3d, and I-5p states, and the CB is mainly composed of the Ag-4d and I-5p orbitals. The partial charge density of Rb$_2$AgI$_3$ (Figure S9c,d) and Cu$^+$-doped Rb$_2$AgI$_3$ (Figure 4c,d) also clearly reflect the orbital distribution of the band edges. These results demonstrate the possibility that excitons are in both [AgI$_4$]$^{3-}$ and [CuI$_4$]$^{3-}$ in Cu$^+$-doped Rb$_2$AgI$_3$. Therefore, the theoretical calculation results are consistent with experimental analysis. When the electrons in the host ground state are excited to high-energy excited states by photons, the electrons undergo energy transfer to the excitation state, which then couple electrons and holes back to the ground state of ES1 and ES2. This is also the reason Cu$^+$-doped Rb$_2$AgI$_3$ produces a more efficient steady-state STE emission.

Remarkably, sky-blue emission was also detected in Cu$^+$-doped Rb$_2$AgI$_3$ SCs under X-ray irradiation. Hence, this material, characterized by broadband emission, high PLQY,

and low self-absorption, emerges as a promising candidate for luminescent applications and holds potential for use as a scintillator. A self-made X-ray detection device is shown in Figure 5a, in which an X-ray source, the imaging object (a capsule containing a metal spring), scintillation film, and a CMOS camera were arranged on an optical table. The scintillation film was prepared by mixing 1.72% Cu^+: Rb_2AgI_3 powder with a PDMS precursor colloidal mixture. When X-ray photons interact with the imaging object, surviving X-ray photons can be detected by the detector, thereby generating a projection image of the object, which results in the clear display of the spring inside the capsule on the computer. Figure S10a shows the internal structure of the imaging object and the corresponding X-ray image. We further evaluated the uniformity and flexibility of X-ray imaging of 1.72% Cu^+: Rb_2AgI_3@PDMS scintillation film. As shown in Figure S10b,c, the translucent film emits bright sky-blue light under 302 nm ultraviolet irradiation, which verifies that the prepared Cu^+-doped Rb_2AgI_3@PDMS film has good uniformity. At the same time, the Cu^+-doped Rb_2AgI_3@PDMS film also shows good flexibility. In terms of the scintillation performance, the RL response of Cu^+-doped Rb_2AgI_3 under X-ray (50 keV) was tested. We derived a light yield of 1.72% Cu^+: Rb_2AgI_3 by comparing its RL integral intensity with that of a reference sample at an equivalent absorbed X-ray energy. The reference scintillator utilized was a CsI: Tl crystal with a known light yield of 54,000 photons/MeV, as shown in Figure 5b. It is not coincidental that there is no noticeable difference from that excited by UV light at 310 nm, suggesting the same radiative recombination pathway under both X-ray and UV excitations. In order to achieve optimal performance in X-ray detection, the RL spectrum should match the response peaks of photodetectors. Remarkably, the RL spectrum of Cu^+-doped Rb_2AgI_3 crystals with blue emission closely aligns with the photodetection efficiency curve of a commercial SiPM, suggesting a notable advantage of Cu^+-doped Rb_2AgI_3 as a scintillator. The response time of Cu^+-doped Rb_2AgI_3 (465 ns) represents another significant advantage as a scintillator material. Generally, a short lifetime results in a small afterglow, thus reducing the SNR of the X-ray imaging.[53] In Table S2, we compared the light yield and decay times of traditional scintillators and Cu-based and Ag-based MHs reported to date. On one hand, by avoiding the use of toxic substances like Tl and expensive rare earth metals like Lu and Ce, we have a competitive advantage in terms of both environmental sustainability and cost effectiveness. On the other hand, as a promising lead-free MH scintillator material, Cu^+-doped Rb_2AgI_3 scintillator typically exhibits relatively shorter lifetimes compared to Cu-based MHs, such as K_2CuCl_3, K_2CuBr_3, Rb_2CuCl_3, and Rb_2CuBr_3.[28−30,54] The microsecond-level lifetimes of these Cu-based MHs limit their applications despite their relatively higher light yield. In contrast, Ag-based MHs have very short lifetimes, but their light yield is not ideal.[55,56] Our research findings indicate that the Cu^+-doped Rb_2AgI_3 scintillator synthesized possesses significant advantages, including relatively shorter decay times and higher light yields. Furthermore, the detection limit also serves as a crucial parameter in evaluating the performance of X-ray scintillators. To determine the X-ray detection limit, RL emission spectra were captured at various dose rates ranging from 8.8 to 83.1 μGy_{air} s^{-1} (Figure 5c), with the RL intensity monotonically increasing as the X-ray dose rates increased. As shown in Figure 5d, Cu^+-doped samples exhibited a low detection limit

of 1.022 μGy_{air} s^{-1} and demonstrated excellent responsiveness to X-rays. Importantly, the obtained result was below the typical dose rate required for X-ray diagnosis (5.5 μGy_{air} s^{-1}).[57] Additionally, spatial resolution is regarded as the key parameter to evaluate imaging resolution. Figure S11 displays the calculated modulation transfer function (MTF) of imagers. At the X-ray dose rate of 83.1 μGy_{air}/s, the spatial resolution of 1.72% Cu^+: Rb_2AgI_3@PDMS scintillation screen is ultimately determined as 10.2 lp mm^{-1} (MTF = 0.2). Figure S12 plots the X-ray response of scintillation films under continuous radiation for 7200 s. The RL intensity exhibits almost no decrease from its initial value, implying excellent radiative stability at a high dose rate. Moreover, the structural and PL emission stabilities of Cu^+-doped Rb_2AgI_3 crystals were further researched. In addition to excellent optical properties, Cu^+-doped Rb_2AgI_3 also exhibits good humidity stability. In comparison to the fresh sample, the XRD pattern of the Cu^+-doped Rb_2AgI_3 sample, exposed to air for 3 months, remained unchanged, with no signs of impurity generation. It indicated the excellent environmental stability of the crystal structure. Besides, the PL intensity of the doped samples was only reduced by approximately 95.62% after three months of exposure to air, demonstrating its robust PL emission stability (Figure S13).

4. CONCLUSIONS

In conclusion, we developed a new kind of nontoxic scintillator, Cu^+-doped Rb_2AgI_3 SCs by a simple temperature-lowering crystallization method. The 1D crystal structure results in a strong quantum confinement in $[AgI_4]^{3-}$ tetrahedra, which gives high PLQY (76.48%) in the sky-blue emission peaked at 490 nm with a large Stokes shift of 180 nm, originating from a STE. For X-ray scintillation properties, Cu^+-doped SCs exhibited a high-light yield of 36,293 photons MeV^{-1}, a repaid scintillation decay time in the nanosecond range (465 ns), and a relatively low detection limit of 1.022 μGy_{air} s^{-1}. The prepared translucent scintillation film was also verified as having good uniformity and flexibility with a high spatial resolution of 10.2 lp mm^{-1}. Future work may involve the fabrication of flexible, large-area scintillation screens using Cu^+-doped Rb_2AgI_3 material, which would further enhance the light yield and practicality of this material. Thus, the high PLQY, considerable light yield, short decay time, good stability, and eco-friendly Cu^+-doped Rb_2AgI_3 will be promising candidates for applications in emitting optoelectronic fields and X-ray imaging.

■ ASSOCIATED CONTENT

Ⓢ Supporting Information

The Supporting Information is available free of charge at https://pubs.acs.org/doi/10.1021/acsomega.4c04077.

> ICP-OES data, PL spectra, absorption spectra, XRD patterns, PLQY measurements, and time-resolved PL decay spectra of undoped and Cu^+-doped Rb_2AgI_3 (PDF)

■ AUTHOR INFORMATION

Corresponding Authors

Xiaoming Li − MIIT Key Laboratory of Advanced Display Material and Devices, School of Materials Science and Engineering, Nanjing University of Science and Technology, Nanjing 210094, China; ⓞ orcid.org/0000-0003-1795-0371; Email: lixiaoming@njust.edu.cn

Wensheng Yang − *State Key Laboratory of Inorganic Synthesis and Preparative Chemistry, College of Chemistry, Jilin University, Changchun 130012, China;* ⊙ orcid.org/0000-0003-2674-6751; Email: wsyang@jlu.edu.cn

Renguo Xie − *State Key Laboratory of Inorganic Synthesis and Preparative Chemistry, College of Chemistry, Jilin University, Changchun 130012, China;* ⊙ orcid.org/0000-0003-0361-3905; Email: renguoxie@jlu.edu.cn

Authors

Jiali Yao − *State Key Laboratory of Inorganic Synthesis and Preparative Chemistry, College of Chemistry, Jilin University, Changchun 130012, China;* ⊙ orcid.org/0000-0001-8259-0662

Dan Huang − *State Key Laboratory of Inorganic Synthesis and Preparative Chemistry, College of Chemistry, Jilin University, Changchun 130012, China*

Xudong Hu − *MIIT Key Laboratory of Advanced Display Material and Devices, School of Materials Science and Engineering, Nanjing University of Science and Technology, Nanjing 210094, China*

Haiming Cheng − *State Key Laboratory of Inorganic Synthesis and Preparative Chemistry, College of Chemistry, Jilin University, Changchun 130012, China*

Dayang Wang − *State Key Laboratory of Inorganic Synthesis and Preparative Chemistry, College of Chemistry, Jilin University, Changchun 130012, China;* ⊙ orcid.org/0000-0003-3678-6677

Complete contact information is available at:
https://pubs.acs.org/10.1021/acsomega.4c04077

Author Contributions

J.Y., D.H., and X.H. contributed equally to this work. The manuscript was written through the contributions of all authors. All authors have their given approval to the final version of the manuscript.

Notes

The authors declare no competing financial interest.

■ REFERENCES

(1) Wang, Y.; Yin, X.; Liu, W.; Xie, J.; Chen, J.; Silver, M. A.; Sheng, D.; Chen, L.; Diwu, J.; Liu, N.; Chai, Z.; Albrecht-Schmitt, T. E.; Wang, S. Emergence of Uranium as a Distinct Metal Center for Building Intrinsic X-ray Scintillators. *Angew. Chem., Int. Ed.* **2018**, *57* (26), 7883−7887.

(2) Durie, B. G. M.; Salmon, S. E. High Speed Scintillation Autoradiography. *Science* **1975**, *190* (4219), 1093−1095.

(3) Maddalena, F.; Tjahjana, L.; Xie, A.; Arramel; Zeng, S.; Wang, H.; Coquet, P.; Drozdowski, W.; Dujardin, C.; Dang, C.; Birowosuto, M. D. Inorganic, Organic, and Perovskite Halides with Nanotechnology for High-Light Yield X- and γ-ray Scintillators. *Crystals* **2019**, *9* (2), 88.

(4) Hofstadter, R. Alkali Halide Scintillation Counters. *Phys. Rev.* **1948**, *74* (1), 100−101.

(5) Nikl, M. Wide Band Gap Scintillation Materials: Progress in the Technology and Material Understanding. *Phys. Status Solidi A* **2000**, *178* (2), 595−620.

(6) Dorenbos, P. Fundamental Limitations in the Performance of Ce^{3+}-Pr^{3+}-and Eu^{2+}-Activated Scintillators. *IEEE Trans. Nucl. Sci.* **2010**, *57* (3), 1162−1167.

(7) Weber, M. J. Inorganic Scintillators: Today and Tomorrow. *J. Lumin.* **2002**, *100* (1−4), 35−45.

(8) Veselova, V. O.; Gajtko, O. M.; Volodin, V. D.; Egorysheva, A. V. Effect of Different Organic Additives on the Shape, Size and Scintillation Properties of $Bi_4Ge_3O_{12}$ Powders Synthesized by the Microwave-Hydrothermal Method. *Adv. Powder Technol.* **2021**, *32* (1), 175−185.

(9) Moseley, O. D. I.; Doherty, T. A. S.; Parmee, R.; Anaya, M.; Stranks, S. D. Halide Perovskites Scintillators: Unique Promise and Current Limitations. *J. Mater. Chem. C* **2021**, *9* (35), 11588−11604.

(10) Liu, X.-K.; Xu, W.; Bai, S.; Jin, Y.; Wang, J.; Friend, R. H.; Gao, F. Metal Halide Perovskites for Light-Emitting Diodes. *Nat. Mater.* **2021**, *20* (1), 10−21.

(11) Xuan, T.; Xie, R.-J. Recent Processes on Light-Emitting Lead-Free Metal Halide Perovskites. *Chem. Eng. J.* **2020**, *393*, 124757.

(12) Lin, K.; Xing, J.; Quan, L. N.; de Arquer, F. P. G.; Gong, X.; Lu, J.; Xie, L.; Zhao, W.; Zhang, D.; Yan, C.; Li, W.; Liu, X.; Lu, Y.; Kirman, J.; Sargent, E. H.; Xiong, Q.; Wei, Z. Perovskite Light-Emitting iodes with External Quantum Efficiency Exceeding 20 Percent. *Nature* **2018**, *562* (7726), 245−248.

(13) Zhou, Y.; Chen, J.; Bakr, O. M.; Mohammed, O. F. Metal Halide Perovskites for X-ray Imaging Scintillators and Detectors. *ACS Energy Lett.* **2021**, *6* (2), 739−768.

(14) Luo, J.; Wang, X.; Li, S.; Liu, J.; Guo, Y.; Niu, G.; Yao, L.; Fu, Y.; Gao, L.; Dong, Q.; Zhao, C.; Leng, M.; Ma, F.; Liang, W.; Wang, L.; Jin, S.; Han, J.; Zhang, L.; Etheridge, J.; Wang, J.; Yan, Y.; Sargent, E. H.; Tang, J. Efficient and Stable Emission of Warm-White Light from Lead-Free Halide Double Perovskites. *Nature* **2018**, *563* (7732), 541−545.

(15) Liu, M.; Pasanen, H.; Ali-Löytty, H.; Hiltunen, A.; Lahtonen, K.; Qudsia, S.; Smått, J.-H.; Valden, M.; Tkachenko, N. V.; Vivo, P. B-Site Co-Alloying with Germanium Improves the Efficiency and Stability of All-Inorganic Tin-Based Perovskite Nanocrystal Solar Cells. *Angew. Chem. Int. Ed.* **2020**, *59* (49), 22117−22125.

(16) Belsky, A. N.; Chevallier, P.; Mel'chakov, E. N.; Pédrini, C.; Rodnyi, P. A.; Vasil'ev, A. N. Luminescence Properties of the $RbCaF_3$ Crystal at X-ray Excitation. *Chem. Phys. Lett.* **1997**, *278* (4−6), 369−372.

(17) Shibuya, K.; Koshimizu, M.; Takeoka, Y.; Asai, K. Scintillation Properties of $(C_6H_{13}NH_3)_2PbI_4$: Exciton Luminescence of an Organic/Inorganic Multiple Quantum Well Structure Compound Induced by 2.0 MeV Protons. *Nucl. Instrum. Methods* **2002**, *194* (2), 207−212.

(18) Chen, Q.; Wu, J.; Ou, X.; Huang, B.; Almutlaq, J.; Zhumekenov, A. A.; Guan, X.; Han, S.; Liang, L.; Yi, Z.; Li, J.; Xie, X.; Wang, Y.; Li, Y.; Fan, D.; Teh, D. B. L.; All, A. H.; Mohammed, O. F.; Bakr, O. M.; Wu, T.; Bettinelli, M.; Yang, H.; Huang, W.; Liu, X. All-Inorganic Perovskite Nanocrystal Scintillators. *Nature* **2018**, *561* (7721), 88−93.

(19) Manser, J. S.; Saidaminov, M. I.; Christians, J. A.; Bakr, O. M.; Kamat, P. V. Making and Breaking of Lead Halide Perovskites. *Acc. Chem. Res.* **2016**, *49* (2), 330−338.

(20) Yan, S.; Liu, S.; Teng, Z.; Li, H.; Chen, W.; Zhou, W.; Qiu, J.; Yu, X.; Wang, S.; Xu, X. High Quality Lead-Free Perovskites toward White Light Emitting Diodes and X-ray Imaging. *J. Mater. Chem. C* **2022**, *10* (43), 16294−16300.

(21) Morad, V.; Shynkarenko, Y.; Yakunin, S.; Brumberg, A.; Schaller, R. D.; Kovalenko, M. V. Disphenoidal Zero-Dimensional Lead, Tin, and Germanium Halides: Highly Emissive Singlet and Triplet Self-Trapped Excitons and X-ray Scintillation. *J. Am. Chem. Soc.* **2019**, *141* (25), 9764−9768.

(22) Xu, X.; Xie, Y.-M.; Shi, H.; Wang, Y.; Zhu, X.; Li, B.-X.; Liu, S.; Chen, B.; Zhao, Q. Light Management of Metal Halide Scintillators for High-Resolution X-ray Imaging. *Adv. Mater.* **2023**, *36* (3), 2303738.

(23) Zhang, Y.; Liu, Y.; Xu, Z.; Ye, H.; Yang, Z.; You, J.; Liu, M.; He, Y.; Kanatzidis, M. G.; Liu, S. Nucleation-Controlled Growth of Superior Lead-Free Perovskite Cs$_3$Bi$_2$I$_9$ Single-Crystals for High-Performance X-ray Detection. *Nat. Commun.* **2020**, *11* (1), 2304.

(24) Zhao, S.; Jia, Z.; Huang, Y.; Qian, Q.; Lin, Q.; Zang, Z. Solvent-Free Synthesis of Inorganic Rubidium Copper Halides for Efficient Wireless Light Communication and X-ray Imaging. *Adv. Funct. Mater.* **2023**, *33* (47), 2305858.

(25) Saeki, K.; Fujimoto, Y.; Koshimizu, M.; Yanagida, T.; Asai, K. Comparative Study of Scintillation Properties of Cs$_2$HfCl$_6$ and Cs$_2$ZrCl$_6$. *Appl. Phys. Express* **2016**, *9* (4), 042602.

(26) Luo, J.-B.; Wei, J.-H.; Zhang, Z.-Z.; He, Z.-L.; Kuang, D.-B. A Melt-Quenched Luminescent Glass of an Organic-Inorganic Manganese Halide as a Large-Area Scintillator for Radiation Detection. *Angew. Chem. Int. Ed.* **2023**, *135* (7), No. e202216504.

(27) Li, D.-Y.; Shang, Y.-B.; Liu, Q.; Zhang, H.-W.; Zhang, X.-Y.; Yue, C.-Y.; Lei, X.-W. 0D Hybrid Indium Halide as a Highly Efficient X-ray Scintillation and Ultra-Sensitive Fluorescent Probe. *Mater. Horiz.* **2023**, *10* (11), 5004−5015.

(28) Gao, W.; Niu, G.; Yin, L.; Yang, B.; Yuan, J.-H.; Zhang, D.; Xue, K.-H.; Miao, X.; Hu, Q.; Du, X.; Tang, J. One-Dimensional All-Inorganic K$_2$CuBr$_3$ with Violet Emission as Efficient X-ray Scintillators. *ACS Appl. Electron. Mater.* **2020**, *2* (7), 2242−2249.

(29) Yang, B.; Yin, L.; Niu, G.; Yuan, J.-H.; Xue, K.-H.; Tan, Z.; Miao, X.-S.; Niu, M.; Du, X.; Song, H.; Lifshitz, E.; Tang, J. Lead-Free Halide Rb$_2$CuBr$_3$ as Sensitive X-ray Scintillator. *Adv. Mater.* **2019**, *31* (44), 1904711.

(30) Zhao, X.; Niu, G.; Zhu, J.; Yang, B.; Yuan, J.-H.; Li, S.; Gao, W.; Hu, Q.; Yin, L.; Xue, K.-H.; Lifshitz, E.; Miao, X.; Tang, J. All-Inorganic Copper Halide as a Stable and Self-Absorption-Free X-ray Scintillator. *J. Phys. Chem. Lett.* **2020**, *11* (5), 1873−1880.

(31) Lian, L.; Zheng, M.; Zhang, W.; Yin, L.; Du, X.; Zhang, P.; Zhang, X.; Gao, J.; Zhang, D.; Gao, L.; Niu, G.; Song, H.; Chen, R.; Lan, X.; Tang, J.; Zhang, J. Efficient and Reabsorption-Free Radioluminescence in Cs$_3$Cu$_2$I$_5$ Nanocrystals with Self-Trapped Excitons. *Adv. Sci.* **2020**, *7* (11), 2000195.

(32) Zhang, M.; Zhu, J.; Yang, B.; Niu, G.; Wu, H.; Zhao, X.; Yin, L.; Jin, T.; Liang, X.; Tang, J. Oriented-Structured CsCu$_2$I$_3$ Film by Close-Space Sublimation and Nanoscale Seed Screening for High-Resolution X-ray Imaging. *Nano Lett.* **2021**, *21* (3), 1392−1399.

(33) Wang, J.-X.; Gutiérrez-Arzaluz, L.; Wang, X.; He, T.; Zhang, Y.; Eddaoudi, M.; Bakr, O. M.; Mohammed, O. F. Heavy-Atom Engineering of Thermally Activated Delayed Fluorophores for High-Performance X-ray Imaging Scintillators. *Nat. Photonics* **2022**, *16* (12), 869−875.

(34) Yao, J.-L.; Zhang, Z.-X.; Sun, X.-Q.; Chang, T.; Guo, J.-F.; Huang, K.-K.; Zeng, H.-B.; Wang, D.-Y.; Yang, W.-S.; Zeng, R.-S.; Li, X.-M.; Xie, R.-G. Doped Emitting Cesium Silver Halides as X-ray Scintillator with Fast Response Time, High Absorption Coefficient, and Light Yield. *Adv. Photon. Res.* **2021**, *2* (9), 2100066.

(35) He, T.; Zhou, Y.; Wang, X.; Yin, J.; Gutiérrez-Arzaluz, L.; Wang, J.-X.; Zhang, Y.; Bakr, O. M.; Mohammed, O. F. High-Performance Copper-Doped Perovskite-Related Silver Halide X-ray Imaging Scintillator. *ACS Energy Lett.* **2022**, *7* (8), 2753−2760.

(36) Kresse, G.; Hafner, J. Ab Initio Molecular Dynamics for Liquid Metals. *Phys. Rev. B: Condens. Matter Mater. Phys.* **1993**, *47* (1), 558−561.

(37) Kresse, G.; Hafner, J. Ab Initio Molecular-Dynamics Simulation of the Liquid-Metal-Amorphous-Semiconductor Transition in Germanium. *Phys. Rev. B: Condens. Matter Mater. Phys.* **1994**, *49* (20), 14251−14269.

(38) Perdew, J. P.; Burke, K.; Ernzerhof, M. Generalized Gradient Approximation Made Simple. *Phys. Rev. Lett.* **1996**, *77* (18), 3865−3868.

(39) Kresse, G.; Joubert, D. From Ultrasoft Pseudopotentials to the Projector Augmented-Wave Method. *Phys. Rev. B: Condens. Matter Mater. Phys.* **1999**, *59* (3), 1758−1775.

(40) Blöchl, P. E. Projector Augmented-Wave Method. *Phys. Rev. B: Condens. Matter Mater. Phys.* **1994**, *50* (24), 17953−17979.

(41) Dudarev, S. L.; Botton, G. A.; Savrasov, S. Y.; Humphreys, C. J.; Sutton, A. P. Electron-Energy-Loss Spectra and the structural Stability of Nickel Oxide: An LSDA+U Study. *Phys. Rev. B: Condens. Matter Mater. Phys.* **1998**, *57* (3), 1505−1509.

(42) Brown, I. D.; Howard-Lock, H. E.; Natarajan, M. The Crystal Structure and Polarised Raman Spectrum of Rb$_2$AgI$_3$. *Can. J. Chem.* **1977**, *55* (9), 1511−1514.

(43) Hull, S.; Berastegui, P. Crystal Structures and Ionic Conductivities of Ternary Derivatives of the Silver and Copper Monohalides—II: Ordered Phases within the (AgX)$_x$-(MX)$_{1-x}$ and (CuX)$_x$-(MX)$_{1-x}$ (M = K, Rb and Cs; X = Cl, Br and I) Systems. *J. Solid State Chem.* **2004**, *177* (9), 3156−3173.

(44) Meng, X.; Wei, Q.; Lin, W.; Huang, T.; Ge, S.; Yu, Z.; Zou, B. Efficient Yellow Self-Trapped Exciton Emission in Sb^{3+}-Doped RbCdCl$_3$ Metal Halides. *Inorg. Chem.* **2022**, *61* (18), 7143−7152.

(45) Varshni, Y. P. Temperature Dependence of the Energy Gap in Semiconductors. *Physica* **1967**, *34* (1), 149−154.

(46) Stadler, W.; Hofmann, D. M.; Alt, H. C.; Muschik, T.; Meyer, B. K.; Weigel, E.; Müller-Vogt, G.; Salk, M.; Rupp, E.; Benz, K. W. Optical Investigations of Defects in Cd$_{1-x}$Zn$_x$Te. *Phys. Rev. B: Condens. Matter Mater. Phys.* **1995**, *51* (16), 10619−10630.

(47) Kang, S.; Kim, Y.; Jang, E.; Kang, Y.; Han, S. Fundamental Limit of the Emission Linewidths of Quantum Dots: An Ab Initio Study of CdSe Nanocrystals. *ACS Appl. Mater. Interfaces* **2020**, *12* (19), 22012−22018.

(48) Zaunbrecher, K. N.; Kuciauskas, D.; Swartz, C. H.; Dippo, P.; Edirisooriya, M.; Ogedengbe, O. S.; Sohal, S.; Hancock, B. L.; LeBlanc, E. G.; Jayathilaka, P. A. R. D.; Barnes, T. M.; Myers, T. H. Impact of Extended Defects on Recombination in CdTe Heterostructures Grown by Molecular Beam Epitaxy. *Appl. Phys. Lett.* **2016**, *109* (9), 091904.

(49) Jiang, F.; Wu, Z.; Lu, M.; Gao, Y.; Li, X.; Bai, X.; Ji, Y.; Zhang, Y. Broadband Emission Origin in Metal Halide Perovskites: Are Self-Trapped Excitons or Ions? *Adv. Mater.* **2023**, *35* (51), 2211088.

(50) Kumar, P.; Creason, T. D.; Fattal, H.; Sharma, M.; Du, M.-H.; Saparov, B. Composition-Dependent Photoluminescence Properties and Anti-Counterfeiting Applications of A$_2$AgX$_3$ (A = Rb, Cs; X = Cl, Br, I). *Adv. Funct. Mater.* **2021**, *31* (48), 2104941.

(51) Li, D.-Y.; Tan, Q.; Ren, M.-P.; Wang, W.-Q.; Zhang, B.-L.; Niu, G.; Gong, Z.; Lei, X.-W. Near-Unity Broadband Luminescent Cuprous Halide Nanoclusters as Highly Efficient X-ray Scintillators. *Sci. China Mater.* **2023**, *66* (12), 4764−4772.

(52) Dai, Y.; Wei, Q.; Chang, T.; Zhao, J.; Cao, S.; Zou, B.; Zeng, R. Efficient Self-Trapped Exciton Emission in Ruddlesden-Popper Sb-Doped Cs$_3$Cd$_2$Cl$_7$ Perovskites. *J. Phys. Chem. C* **2022**, *126* (27), 11238−11245.

(53) Crepp, J. R.; Letchev, S. O.; Potier, S. J.; Follansbee, J. H.; Tusay, N. T. Measuring Phase Errors in the Presence of Scintillation. *Opt. Express* **2020**, *28* (25), 37721−37733.

(54) Zhang, F.; Lin, Z.; Xie, L.; Li, X.; Lu, B.; Zhao, Z.; Jiang, T.; Wang, M.; Wu, Y.; Zhou, Q.; Xiao, J.; Chen, B.; Wang, Y. Blue-Violet Emitting K$_2$CuCl$_3$ Compound: Facile Synthesis, Photoluminescence and Radioluminescence Properties. *J. Mater. Sci.* **2022**, *57* (22), 10260−10270.

(55) Zhang, Z.; Guo, X.; Huang, K.; Sun, X.; Li, X.; Zeng, H.; Zhu, X.; Zhang, Y.; Xie, R. Lead-Free Bright Yellow Emissive Rb$_2$AgCl$_3$ Scintillators with Nanosecond Radioluminescence. *J. Lumin.* **2022**, *241*, 118500.

(56) Zhang, M.; Wang, X.; Yang, B.; Zhu, J.; Niu, G.; Wu, H.; Yin, L.; Du, X.; Niu, M.; Ge, Y.; Xie, Q.; Yan, Y.; Tang, J. Metal Halide Scintillators with Fast and Self-Absorption-Free Defect-Bound Excitonic Radioluminescence for Dynamic X-ray Imaging. *Adv. Funct. Mater.* **2021**, *31* (9), 2007921.

(57) Han, K.; Jin, J.; Su, B.; Qiao, J.; Xia, Z. Promoting Single Channel Photon Emission in Copper(I) Halide Clusters for X-ray Detection. *Adv. Opt. Mater.* **2022**, *10* (20), 2200865.